

# Bringing the Galaxy’s dark halo to life

T. Piffl<sup>1</sup>\*, Z. Penoyre<sup>2</sup>, J. Binney<sup>1</sup>

<sup>1</sup>Rudolf Peierls Centre for Theoretical Physics, Keble Road, Oxford OX1 3NP, UK

<sup>2</sup>Trinity Hall, University of Cambridge, Trinity Lane, Cambridge CB2 1TJ, UK

submitted to MNRAS on 19th January 2015

## ABSTRACT

We present a new method to construct fully self-consistent equilibrium models of multi-component disc galaxies similar to the Milky Way. We define distribution functions for the stellar disc and dark halo that depend on phase space position only through action coordinates. We then use an iterative approach to find the corresponding gravitational potential. We study the adiabatic response of the initially spherical dark halo to the introduction of the baryonic component and find that the halo flattens in its inner regions with final minor-major axis ratios  $q = 0.75 – 0.95$ . The extent of the flattening depends on the velocity structure of the halo particles with radially biased models exhibiting a stronger response. In this latter case, which is according to cosmological simulations the most likely one, the new density structure resembles a “dark disc” superimposed on a spherical halo. We discuss the implications of these results for our recent estimate of the local dark matter density.

The velocity distribution of the dark-matter particles near the Sun is very non-Gaussian. All three principal velocity dispersions are boosted as the halo contracts, and at low velocities a plateau develops in the distribution of  $v_z$ . For models similar to a state-of-the-art Galaxy model we find velocity dispersions around  $155 \text{ km s}^{-1}$  for  $v_z$  and the tangential velocity,  $v_\varphi$ , and  $140 – 175 \text{ km s}^{-1}$  for the in-plane radial velocity,  $v_R$ , depending on the anisotropy of the model.

**Key words:** galaxies: kinematics and dynamics

## 1 INTRODUCTION

It is now generally accepted that most of the rest mass in the Universe is contained in a type of “dark matter” that is incapable of electromagnetic interactions. Dark matter began to cluster gravitationally earlier than baryonic matter because it was decoupled from the cosmic radiation bath, which at redshifts  $\gtrsim 1000$  provided abundant pressure. Hence the formation of a galaxy starts with the accumulation of dark matter to form the dark halo. When and how baryons accumulated in the gravitational potential wells of dark halos is ill understood. In the simplest picture, they simply fell in dissipatively and formed stars near each halo’s centre, but this picture is inconsistent with the small fraction of baryons that are now in stars rather than intergalactic gas. Several lines of evidence indicate that the release of nuclear energy by early stars strongly attenuated the infall of baryons, thus increasing the extent to which galaxies are dark-matter dominated.

The least dark-matter dominated galaxies are ones with luminosities similar to that,  $L_*$ , of our Galaxy: dwarf galax-

ies are very strongly dark-matter dominated and stars play such a subsidiary role in the most massive dark-matter halos, those of galaxy groups and clusters, that we do not even recognise these halos as galaxies. Yet even in galaxies such as ours, it may be argued that the baryons have played a very subordinate role. Measurements of the optical depth to microlensing of stars located less than  $\sim 10 \text{ deg}$  from the Galactic centre imply that a significant majority of the mass inside  $\sim 3 \text{ kpc}$  is concentrated in stars (Binney & Evans 2001; Bissantz et al. 2004). But the majority of the gravitational force that holds the Sun in its orbit comes from dark matter (e.g. Piffl et al. 2014, hereafter P14), and the dominance of dark matter increases sharply with increasing distance from the centre. Moreover, in galaxies such as ours and M33, we have reason to believe that most baryons accumulated in the potential well of the dark halo quiescently, forming a disc in centrifugal equilibrium (Mo et al. 1998). In our Galaxy, but not in M33, the central portion of the disc became unstable to the formation of a strong bar, which then buckled to form the Galaxy’s present bar/bulge (Combes & Sanders 1981; Raha et al. 1991).

A dark halo will respond to the quiescent accumulation of baryons in a disc by distorting adiabatically: that

\* E-mail: tilmann.piffl@physics.ox.ac.uk

is, the orbit of each dark-matter particle will evolve in such a way that its action integrals  $J_r$ ,  $J_\phi$  and  $J_z$  will be constant, with the consequence that the density of dark-matter particles in action space,  $f(\mathbf{J})$ , is unaffected by the accumulation of baryons and the resulting evolution of the galaxy's gravitational potential  $\Phi(\mathbf{x})$  (e.g. Binney & Tremaine 2008, §4.6.1). The constancy of  $f(\mathbf{J})$  is enormously useful because the gravitational clustering of dark matter in isolation can be simulated with confidence, so we know what dark halos would now populate the Universe if there were no baryons. That is, from dark-matter only simulations we can infer what  $f(\mathbf{J})$  would be in the absence of baryons, and the adiabatic principle assures us that  $f(\mathbf{J})$  will be unchanged by the quiescent infall of baryons in the observed quantities. Hence the adiabatic principle allows us to predict the present structures of galaxies before we understand the complex processes that resulted in the quiescent accumulation of baryons.

This general idea was appreciated at an early stage in the development of the cold dark matter (CDM) cosmological paradigm (Blumenthal et al. 1986), but until recently we have lacked the technology required to exploit it fully. The key to its exploitation is the ability to compute the action vector as a function  $\mathbf{J}(\mathbf{x}, \mathbf{v})$  of ordinary phase-space coordinates  $(\mathbf{x}, \mathbf{v})$ , for then it is possible to compute the dark-matter density

$$\rho_{\text{DM}}(\mathbf{x}) = (2\pi)^3 \int d^3\mathbf{v} f[\mathbf{J}(\mathbf{x}, \mathbf{v})] \quad (1)$$

at any location  $\mathbf{x}$ .

In an axisymmetric potential  $\Phi$  one action,  $J_\phi = L_z$ , is simply the component of angular momentum parallel to the potential's symmetry axis, and in a spherical potential  $J_z = L - |L_z|$ , where  $L$  is the length of the angular-momentum vector  $\mathbf{L}$ . Blumenthal et al. (1986) estimated the response of a dark halo to the accumulation of baryons by assuming that all dark-matter particles are on circular orbits, so  $J_r = 0$ . A more realistic estimate of halo response was obtained by Sellwood & McGaugh (2005), who lifted the restriction  $J_r = 0$  to circular orbits but retained the assumption of spherical symmetry. The latter is awkward because the basic picture is of baryons accumulating in a disc, which will immediately break any pre-existing spherical symmetry of the dark halo.

In this paper we lift the assumption of spherical symmetry, so we are able to compute how the introduction of the disc deforms an initially spherical dark halo into a more centrally concentrated, oblate structure. We are, moreover, able to predict the full, three-dimensional distribution of the velocities of dark-matter particles at any point in the Galaxy, in particular at the Sun. These distributions are triaxial and give non-Maxwellians speed distributions.

## 2 METHODOLOGY

Our strategy is to adopt DFS  $f(\mathbf{J})$  for the Galaxy's stellar disc and dark halo and to solve for the gravitational potential  $\Phi(\mathbf{x})$  that these self-consistently generate in the presence of given density distributions for the bulge and gas disc. We now describe our algorithm for the determination of  $\Phi(\mathbf{x})$ , which an extension of the methodology used by (Binney 2014, hereafter B14) to compute the observables of a flattened isochrone from an adopted DF  $f(\mathbf{J})$ .

### 2.1 Iterative scheme

B14 started from a guess  $\Phi_0$  at the self-consistent potential. Using this guess and equation (1) he determined the density on a grid in the meridional  $(R, z)$  plane, and then solved Poisson's equation for the corresponding potential  $\Phi_{1/2}(R, z)$ . From this he made an improved guess

$$\Phi_1(R, z) = (1 + \alpha)\Phi_{1/2}(R, z) - \alpha\Phi_0(R, z) \quad (2)$$

at the self-consistent potential, where  $\alpha \lesssim 0.5$  is parameter chosen to maximise the speed of convergence of the sequence of potentials  $\Phi_i$  to the self-consistent potential.

The procedure just described involves a grid of points in the  $Rz$  plane at which the density is evaluated. Since the spatial scales of the disc and the dark halo are very discrepant, it is not cost-effective to use the same grid for both components: the grid would have to be fine enough to resolve the  $\lesssim 0.1$  kpc structure of the disc and extensive enough to cover the dark halo, which has a significant amount of mass  $\gtrsim 100$  kpc from the Galactic centre. Hence for each component  $\gamma$  we use a different grid, and on this grid we store estimates of the density  $\rho_\gamma$  of that component and the contribution  $\Phi_\gamma$  that it makes to the total gravitational potential<sup>1</sup>

$$\Phi_{\text{tot}}(R, z) = \sum_{\text{components } \gamma} \Phi_\gamma(R, z). \quad (3)$$

Evaluation of the density of a single component involves evaluation of the actions  $\mathbf{J}(\mathbf{x}, \mathbf{v})$  and in this evaluation we use  $\Phi_{\text{tot}}$  and the ‘Stäckel Fudge’ of Binney (2012). Having evaluated the density  $\rho_\gamma$  of a component throughout the component's grid, we solve Poisson's equation for the corresponding potential  $\Phi_\gamma$ . The values of  $\Phi_\gamma$  at an arbitrary point  $(R, z)$  is obtained by interpolation on the values stored on the component's grid.

We start by determining the self-consistent density and potential implied by the adopted dark-halo DF when the halo is isolated. Then our first trial potential for the whole Galaxy,  $\Phi_{\text{tot}}$ , is the sum of this potential and the potentials of the bulge, gas disc and double-exponential stellar disc. We now compute the density of the dark halo in  $\Phi_{\text{tot}}$ , and solve for the corresponding potential  $\Phi_{\text{DM}}$  and use this to update  $\Phi_{\text{tot}}$ . Then we compute the density  $\rho_*$  of the stellar disc in this estimate of  $\Phi_{\text{tot}}$  and use the corresponding potential  $\Phi_*$  to update  $\Phi_{\text{tot}}$ . Then we compute the density of the dark halo in the updated  $\Phi_{\text{tot}}$ , and so on until successive estimates of  $\Phi_{\text{tot}}$  differ negligibly. This occurs after no more than four computations of the density of each component.

### 2.2 Target model

Our aim is to reproduce one of the Galaxy models presented by P14 – we shall refer to this as the ‘target’ model. Since the potentials of the discs cause a dark halo that is spherical when isolated to flatten in its inner region, we chose to target the model in P14 that has a mildly flattened dark halo (minor-major axis ratio  $q = 0.8$ ). Moreover, P14 remark that comparison of their results with those of Bienaymé et al. (2014) favours a flattened model with axis ratio  $q \simeq 0.8$ . This model was described by P14 (cf. their figures 9, 10 and

<sup>1</sup> We actually store coefficients of Legendre-polynomial expansions and store also radial derivatives.

**Table 1.** Parameters for our target Galaxy mass model.

		Gas disc	Thin disc	Thick disc
$\rho_0$	[ $M_\odot \text{ kpc}^{-3}$ ]	$8.73 \times 10^7$	$5.32 \times 10^8$	$2.74 \times 10^8$
$R_d$	[kpc]	5.16	2.58	2.58
$z_d$	[kpc]	0.04	0.20	0.67
$R_{\text{hole}}$	[kpc]	4	0	0
		Bulge	Dark halo	
$\rho_{0,b}$	[ $M_\odot \text{ kpc}^{-3}$ ]	$9.49 \times 10^{10}$	$1.96 \times 10^7$	
$r_{0,b}$	[kpc]	0.075	15.54	
$r_{\text{cut},b}$	[kpc]	2.1	$10^5$	
$q_b$		0.5	0.8	
$\gamma_b$		0	1	
$\beta_b$		1.8	3	

**Table 2.** Parameters for stellar disc DF.

		Thin disc	Thick disc
$\sigma_r$	$\text{km s}^{-1}$	33.9	50.5
$\sigma_z$	$\text{km s}^{-1}$	25.0	48.9
$R_d$	kpc	2.58	2.58
$R_{\sigma,r}$	kpc	9	12.9
$R_{\sigma,z}$	kpc	9	4.1
$F_{\text{thick}}$	-	-	0.455

11), but they did not specify its parameters. Table 1 contains the parameters of the model's three-dimensional mass distribution. We refer the reader to P14 for the functional forms of the density laws.

### 3 THE DFS

#### 3.1 The stellar disc

For the stellar disc we adopt the DF that P14 found to be consistent with current data, especially the kinematics of giants stars included in the RAdial Velocity Experiment (RAVE Steinmetz et al. 2006). The functional form of the DF, which is made up of contributions from the thick disc and each coeval cohort of thin-disc stars, is given in P14. For brevity it is not repeated here. Table 2 gives the values of the parameters in the stellar disc DF.

We did make one minor change to the functional form of the DF: we imposed a lower limit, 1 kpc, on the circular radius  $R_c(J_\phi)$  at which the epicycle frequencies are evaluated. Implicitly this introduces an upper limit on the frequencies  $\kappa(J_\phi)$ , etc., that appear in the DF. Crucially, after the limit has been imposed these functions remain well-defined functions of the actions, so the legitimacy of the DF is not undermined. But on account of the limit, the frequencies employed in the DF differ from the epicycle frequencies at low  $J_\phi$ . Imposing the limit has negligible impact on the structure of the disc near the Sun; its material impact is at small radii, where the steep rise in the epicycle frequencies as the Galactic centre is approached would otherwise depress the disc's density in an unphysical way. Table 2 gives the values of the parameters in the disc DF.

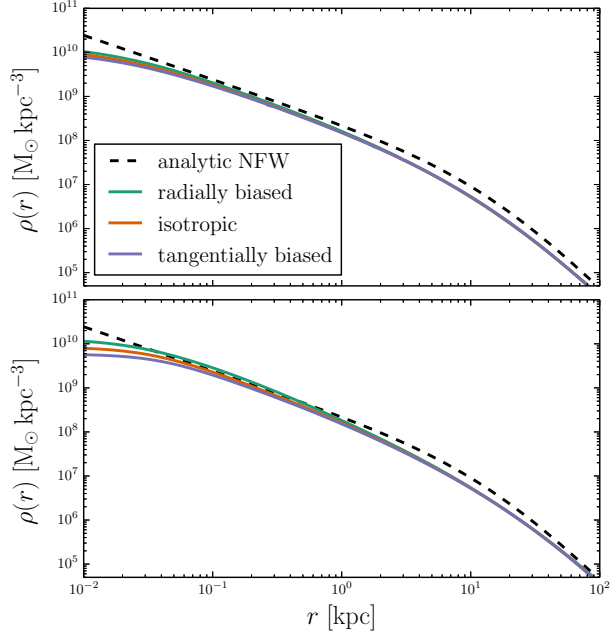


**Figure 1.** Left panel: Density profiles computed from the dark halo DFs evaluated in the analytic NFW potential (coloured lines). The associated analytic NFW density profile is shown as a black dashed line. Right panel: density profiles of the isolated halo models after the potential has been updated to the self-consistently generated one.

#### 3.2 The stellar halo

P14 used a DF  $f(\mathbf{J})$  also for the stellar halo, but we omit this component because it has negligible mass and serves only to improve fits to the stellar kinematics at small  $|v_\phi|$ .

#### 3.3 The dark halo

Pontzen & Governato (2013) have fitted DFs to dark halos formed in dark-matter only cosmological simulations. Unfortunately, the DFs they fitted are not usable here because they have the form  $f(E, L)$ : a DF that describes one component of a composite model with a self-consistently generated potential cannot have energy in its argument list.

The dark halo of the target model has the radial density profile of the classic NFW profile (Navarro et al. 1996). Posti et al. (2014) found a simple DF  $f(\mathbf{J})$  that self-consistently generates a spherical model that has almost exactly an NFW profile. This model is essentially isotropic near its centre, and becomes mildly radially biased beyond its scale radius. For the dark halo we adopt DFs that are based on the form proposed by Posti et al. (2014) even though these DFs do not generate an NFW profile in the presence of the stellar disc. Consequently, the circular-speed curves of our final models are not consistent with the observed tangent velocities. The normalisation of the dark-halo DF (and thus the halo's total mass) is chosen to match the circular speed,  $v_{\text{circ}}(R_0)$ , in the target model at the solar radius  $R_0$ .

We now specify three different dark-halo DFs that cover

**Table 3.** DF parameters for the dark halo.

Parameter	Radially biased	Isotropic	Tangentially biased
$\alpha$	5/3	5/3	5/3
$\beta$	2.9	2.9	2.9
$J_0$	47.3	155	218
$J_{\text{core}}$	0.00025	0.0001	0.0002
$b$	8	1	0.125

the possibilities that the velocity distribution of dark-matter particles is isotropic or radially or tangentially biased. We write

$$f(\mathbf{J}) = \frac{N}{J_0^3} \frac{[1 + J_0/(J_{\text{core}} + h(\mathbf{J}))]^{\alpha}}{[1 + h(\mathbf{J})/J_0]^{\beta}}, \quad (4)$$

where  $N$  is a normalisation constant,  $\alpha$  and  $\beta$  are constants that define the exponents of inner and outer power-law slopes of the density profile,  $J_0$  is a constant that controls the transition between the two. The constant  $J_{\text{core}}$  is a small number required to keep the central density finite. Finally,

$$h(\mathbf{J}) \equiv \frac{1}{A} J_r + \frac{1}{B} \frac{\Omega_{\varphi}}{\kappa} (|J_{\varphi}| + J_z) \quad (5)$$

is an (approximately) homogeneous function<sup>2</sup> of  $\mathbf{J}$  of order unity with

$$A = b_0 + (b - b_0) \tanh^2 \left( \frac{|L_z| + J_z}{J_r + |L_z| + J_z} \right), \quad (6)$$

$$B = b_0 + (1 - b_0) \tanh^2 \left( \frac{|L_z| + J_z}{J_r + |L_z| + J_z} \right) \quad (7)$$

and  $b_0 = (1+b)/2$ . In the Appendix we explain why realistic velocity distributions are obtained only when the values  $A$  and  $B$  are functions of the actions.

The parameter  $b$  controls the model's velocity anisotropy. For  $b = 1$  we obtain a near-isotropic model, while values below (above) unity yield tangentially (radially) biased models. The quantities  $\kappa$  and  $\Omega_{\varphi}$  are epicycle and azimuthal frequencies in the self-consistent spherical model evaluated at the radius  $R_c$  of a circular orbit with angular momentum

$$J_{\text{tot}} \equiv J_r + |J_{\varphi}| + J_z. \quad (8)$$

We take the argument of  $R_c$  to be  $J_{\text{tot}}$  to make it an approximate function of energy, so  $R_c$  does not become small, and the epicycle frequencies large, for stars on eccentric and/or highly inclined orbits with small  $|J_{\varphi}|$ .

Following Posti et al. (2014), we set the exponents  $\alpha$  and  $\beta$  to 5/3 and 2.9, respectively, to obtain a good approximation to the NFW density profile. Table 3 lists all the adopted values of the parameters that define the halo's DF. They generate a halo that (a) closely approximates the NFW profile when the halo is isolated, and (b) in the presence of the discs and bulge has a flattening interior to the Sun similar to that of the target model's dark halo.

Once we have obtained a self-consistent model of an isolated halo, we freeze the dependence of  $R_c$  on its argument,

<sup>2</sup> Posti et al. (2014) argued that  $h(\mathbf{J})$  should be a homogeneous function of  $\mathbf{J}$ , i.e. they required that  $h(a\mathbf{J}) = a h(\mathbf{J})$ .

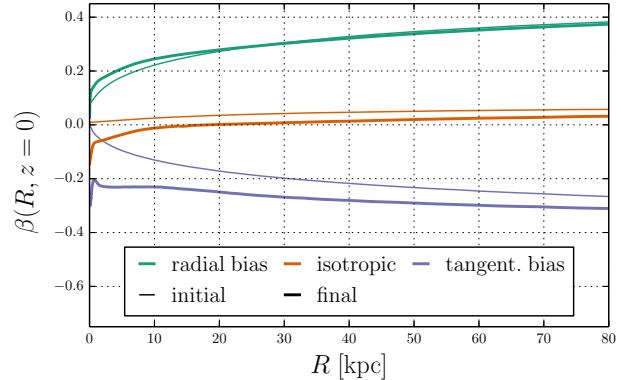


**Figure 2.** Velocity anisotropy of the dark-matter particles as a function of radius in the equatorial plane.

so while we relax  $\Phi_{\text{tot}}$  onto the potential that is jointly generated by all the Galaxy's components, the DF stays exactly the same function of  $\mathbf{J}$ . It is essential to freeze the function  $f(\mathbf{J})$  during the introduction of the discs and the bulge if one seeks to learn how the halo is distorted by the gravitational fields of its companions.

### 3.4 The bulge

We could adopt a DF  $f(\mathbf{J})$  for the final Galactic component, the bulge, but we do not do so for two reasons. First, the bulge contains a rotating bar and at present we cannot represent such an object with a DF  $f(\mathbf{J})$  (but see Sanders & Binney 2014, for a non-rotating triaxial example). Second, we are primarily interested in the structure of the dark halo in the vicinity of the Sun, which should be well recovered using an axisymmetrised form of the bulge. Hence we represent the bulge by a fixed density distribution. We also represent the Galaxy's gas disc by a fixed density distribution.

## 4 RESULTS

### 4.1 Isolated halos

We consider three halo DFs, which differ only in the value of the parameter  $b$ : we set  $b = 0.125$  to generate a tangentially biased model,  $b = 1$  for a nearly isotropic model, and  $b = 8$  for a radially biased model. The left panel of Fig. 1 shows the density profiles generated by the three DFs in the analytic NFW potential (which has no core). The DF parameters were optimised to provide a good match between these density profiles and that of the NFW halo fitted by P14. The right panel of Fig. 1 shows the radial density profiles of these models after the potential has relaxed to self-consistency. (Fitting a self-consistent DF-potential pair to the analytic profile directly is conceptually straightforward, but computationally expensive, and is beyond the scope of this paper.)

The thin curves in Fig. 2 show the anisotropy parameter

$$\beta_a \equiv 1 - \frac{\langle v_t^2 \rangle}{2 \langle v_r^2 \rangle} \quad (9)$$

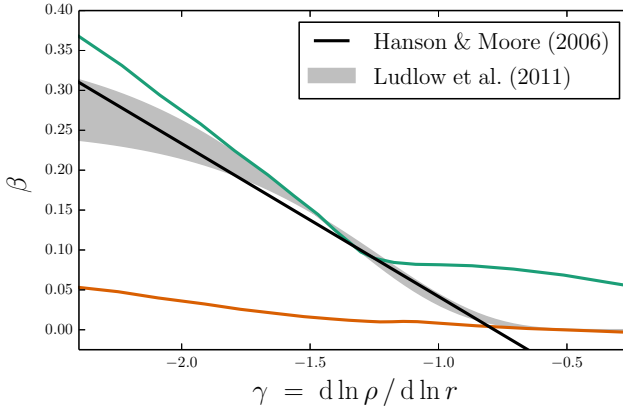


**Figure 3.** Density slope – velocity anisotropy relation for our radially biased (turquoise) and isotropic models (orange) as well as predictions from cosmological dark matter-only simulations.

for the initial isolated halo as a function of radius in the  $xy$  plane. To provide some context, Fig. 3 shows the same as a function of the slope of the logarithmic density profile for two of these models. The grey band shows the range of such dependency found by Ludlow et al. (2011) from cosmological simulations, while the black line shows the linear dependence that Hansen & Moore (2006) found described cosmologically simulated halos well. We see that our isotropic and radially biased models bracket the empirical results well, except possibly at the smallest values of  $|\gamma|$ , which occur at the centre of a halo.

#### 4.2 Halo distortion

The introduction of the baryonic components causes the initially spherical dark halo to contract. The end point of this contraction should coincide perfectly with what we would have found had we slowly grown the baryonic components in a live N-body simulation of the halo. The almost coincident heavy curves in the upper panel of Fig. 4 show the final, relaxed dark-matter density profiles in the disc ( $xy$ ) plane. Even though the central parts of the initial profiles differ, with the radially-biased model being most cuspy (light full curves in the upper panel), the final profiles are very similar. The full curves in the lower panel of Fig. 4 show the ratio of initial to final density at each radius. We see that in all three cases (radial bias, isotropic, tangential bias), the central density increases by more than a factor 8.

This figure shows (i) that at  $r \lesssim 3$  kpc the baryonic component distorts the dark halo substantially, and (ii) that the variation of the initial density profiles with the anisotropy parameter  $b$  is just what is required to ensure that the three profiles coincide after the baryons have been added: as Sellwood & McGaugh (2005) showed, the tangentially biased halo is more strongly compressed than the radially-biased halo, so before the barons are added its density needs to be lower than that of the radially-biased halo.

The dotted curves in the upper panel of Fig. 4 show the profiles one obtains when one starts with the three isolated halos and applies to these objects the classic adiabatic contraction formalism of (Blumenthal et al. 1986). This for-

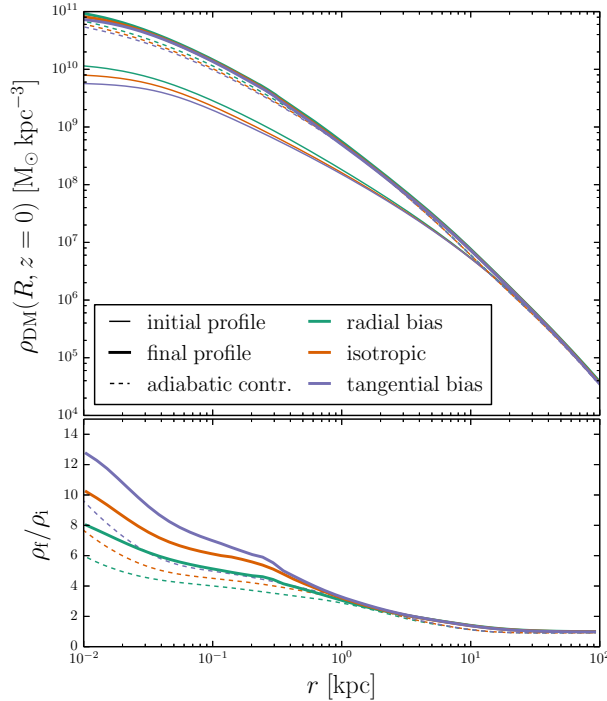


**Figure 4.** Upper panel: solid thin lines show the spherically symmetric density profiles of halos in isolation, while thick lines show the density profiles in the  $xy$ -plane after the halos have been contracted by introducing the baryons. The dotted lines show the profiles obtained by contracting the original models with the classic adiabatic prescription. Lower panel: final density divided by initial density when the contraction is done properly (full curves) and using the classical prescription (dotted curves).

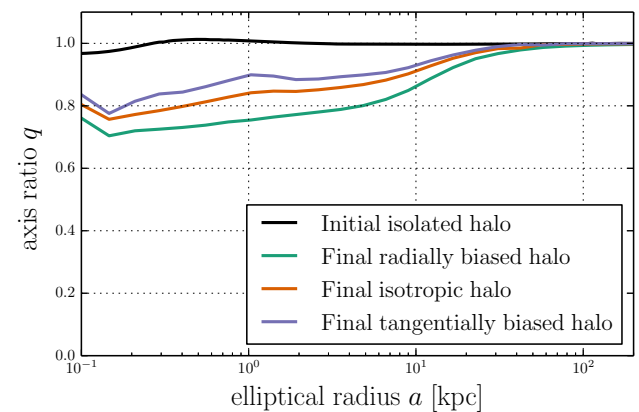


**Figure 5.** Minor-major axis ratio of the halo component as a function of elliptical radius  $a = \sqrt{R^2 + (z/q)^2}$ .

malism is based on the fiction that all dark matter particles are on circular orbits, i.e. an extreme case of tangential bias. From the lower panel of Fig. 4 we see that the analytic prediction is in excellent agreement with our results for  $r > 1$  kpc, but under-estimates the contraction for smaller radii.

We can for the first time study how the flattened baryon

distribution breaks the spherical symmetry of the halo, and pulls it towards the plane – hitherto analytic prescriptions for adiabatic distortion have been restricted to the spherical case. Fig. 5 shows the axis ratio of the final dark halo as a function of elliptical radius. We see that the radially biased halo is most strongly flattened by the baryons – its axis ratio does not rise above 0.8 until near  $R_0$ . The axis ratio of the initially nearly isotropic halo rises more gradually from similar values at  $\sim 0.2$  kpc to  $\sim 0.9$  near the Sun. We emphasise that these axis ratios are arising naturally and are *not* related to our choice of a target model with a similarly flattened halo. In fact, we found very similar axis ratios in test runs using the P14 model with a spherical halo and then inspired by these results chose to use the flattened model as a target.

Fig. 6 finally shows the relative changes in the halo density distributions in the  $(R, z)$ -plane. In particular in the radially biased case the difference between the self-consistent halo and the original spherical model could also be interpreted as a “dark disc” that formed during the collapse. Pillepich et al. (2014) considered anisotropic contraction when analysing a cosmological simulation of the formation of a disc galaxy similar to the Milky Way. They find  $\sim 30$  per cent enhanced dark-matter density at the Sun compared to a dark matter-only run. This is in excellent agreement with our findings.

Previously, dark discs were predominantly associated with the capture of satellites onto highly inclined orbits and their subsequent tidal shredding (Read et al. 2008, 2009; Ruchti et al. 2014; Read 2014). A dark disc formed thus would differ from the density enhancement near the plane found here in that it would have a clear sense of circulation around the halo’s spin axis while our density enhancements are non-rotating. Pillepich et al. (2014) already showed that for a rather quiescent merger history as expected for our Galaxy, the dark disc due to adiabatic contraction is the dominant contributor.

### 4.3 DM velocity distributions

We now examine the velocity distribution of the dark matter particles within the Galactic plane of our models. Fig. 2 shows the radial dependence of the classical anisotropy parameter (equation 9) before and after adiabatic contraction. The most significant changes are in the innermost regions where the baryonic discs are dominant. In the radially biased case (turquoise curves), the anisotropy is practically unchanged by the contraction at larger radii. In the other two cases the anisotropy is changed significantly, but no qualitative changes are observable outside the disc region.

The sensitivity of particle detectors typically depends on the speed of the particles to be detected. Even though no finite collisionless stellar system can have a Maxwellian velocity distribution, the speed distribution of dark-matter particles at the Sun has in the past been assumed to be the Maxwellian distribution in which the velocity dispersion coincides with the velocity dispersion predicted by stellar dynamics. Hence it is interesting to compare the speed distributions of our models with the corresponding Maxwellian distributions.

Each full curve in the left panel of Fig. 7 shows the distribution over speed of the dark-matter particles in one

**Table 4.** Local dark matter velocity dispersions

model	$\sigma_{v_R}$ km s $^{-1}$	$\sigma_{v_\varphi}$ km s $^{-1}$	$\sigma_{v_z}$ km s $^{-1}$
radially biased	174	150	154
isotropic	154	154	157
tangent. biased	141	156	158

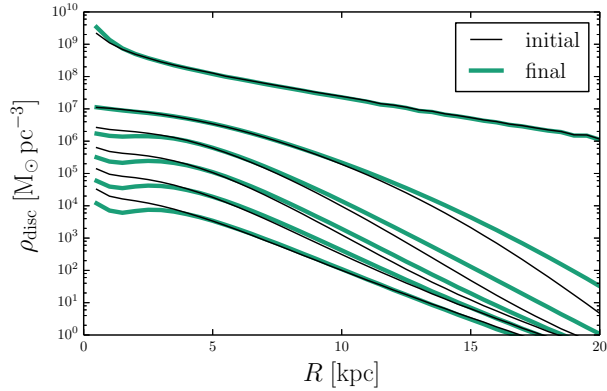


**Figure 9.** Density profile of the stellar disc in slices of constant  $z$  before and after the dark halo’s response to the presence of the disc. The line pairs correspond to heights above the Galactic plane from 0 kpc (up-most almost identical lines) to 10 kpc (lowest lines) in steps of 2 kpc.

of our models, while the dashed curve of the same colour shows the Maxwellian distribution that has the same velocity dispersion. In the tangentially biased model the speed distribution is more sharply peaked than the corresponding Maxwellian, and *vice versa* in the radially biased model. In all three models the speed distribution falls below the Maxwellian at large  $v$  because it falls to zero at or before the escape speed. The right panel of Fig. 7 shows the ratio of the model speed distribution to the corresponding Maxwellian. We see that the chances of detecting dark matter with a speed-sensitive detector are significantly higher in the radially biased case than in the tangentially biased case. Fortunately, N-body simulations imply that dark halos are radially biased (e.g. Hansen & Moore 2006; Ludlow et al. 2011; Pontzen & Governato 2013).

Fig. 8 shows the distributions of the three velocity components (after marginalising over the other two components) of dark-matter particles at the location  $\mathbf{x} = (R_0, 0)$  of the Sun.<sup>3</sup> The non-Gaussian nature of these velocity distributions is evident. In all cases adiabatic contraction of the halo broadens the distributions for the same reason gas that is adiabatically compressed heats up. As the  $v_z$ -direction broadens, its top becomes remarkably flat. The dispersions of the distributions are listed in Table 4.

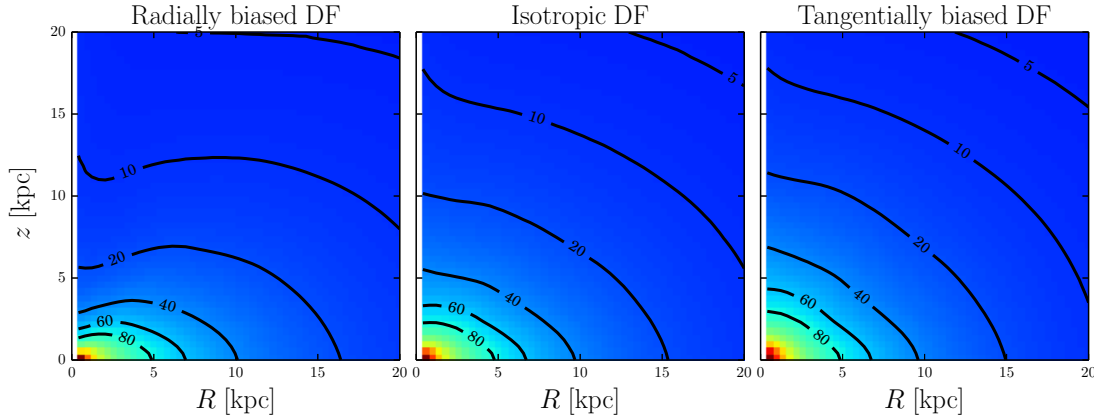


**Figure 6.** Relative density difference of the dark halo component before and after the adiabatic contraction,  $(\rho_{\text{final}} - \rho_{\text{ini}})/\rho_{\text{ini}}$ , due to the baryonic components. Each panel corresponds to a model with different velocity anisotropy as indicated above the panels. The contour lines mark locations where the density has increased similarly by a given fraction in per cent as indicated on the lines.

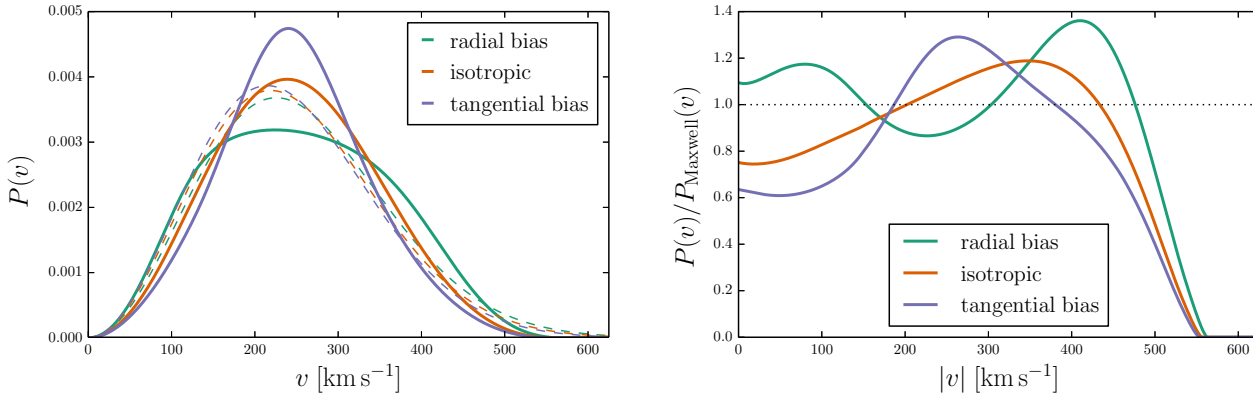


**Figure 7.** Speed distributions of the final models. Left: the distribution of speeds of dark-matter particles in the three models are shown as the full curves, while the dashed curves show the Maxwellian distributions with the same dispersion. Right: each full curve shows the ratio of a speed distribution to the Maxwellian distribution that has the same velocity dispersion.

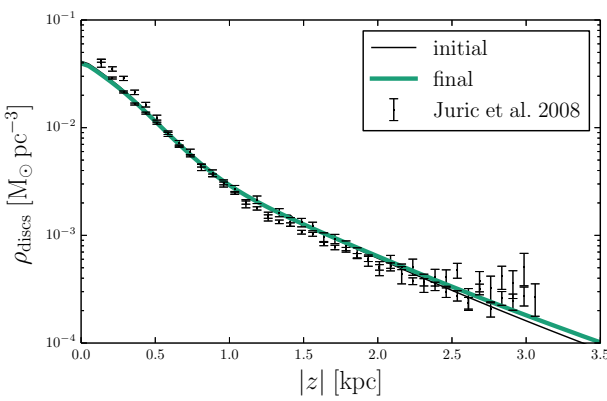


**Figure 10.** Vertical density profile of the stellar disc in the solar cylinder before and after the response of the halo to the presence of the disc. The star count data from Jurić et al. (2008) have been re-normalised (shifted vertically) to allow a comparison to the model.

#### 4.4 The stellar disc

Figs. 9 and 10 show the stellar density structure in the case of the radially biased halo by showing density profiles at fixed  $z$  and  $R_0$ , respectively, for the disc DF evaluated in the target Galaxy potential in black, and in turquoise the same profiles after making the halo self-consistent. The differences between these profiles are significant only in the outer disc regions (Fig. 9) where the final halo is rounder than that of the target distribution. In the solar cylinder the density profiles agree extremely well (Fig. 10), so the final model still provides an excellent match to the star count data of Jurić et al. (2008) to which the target model was fitted.

#### 4.5 Rotation curve

Our P14 target model was fitted to data constraining the Galaxy's rotation curve using an NFW halo profile. As we

<sup>3</sup> We adopt  $R_0 = 8.3$  kpc. The distributions at the actual solar position 14 to 25 pc above the Galactic plane are indistinguishable from these.

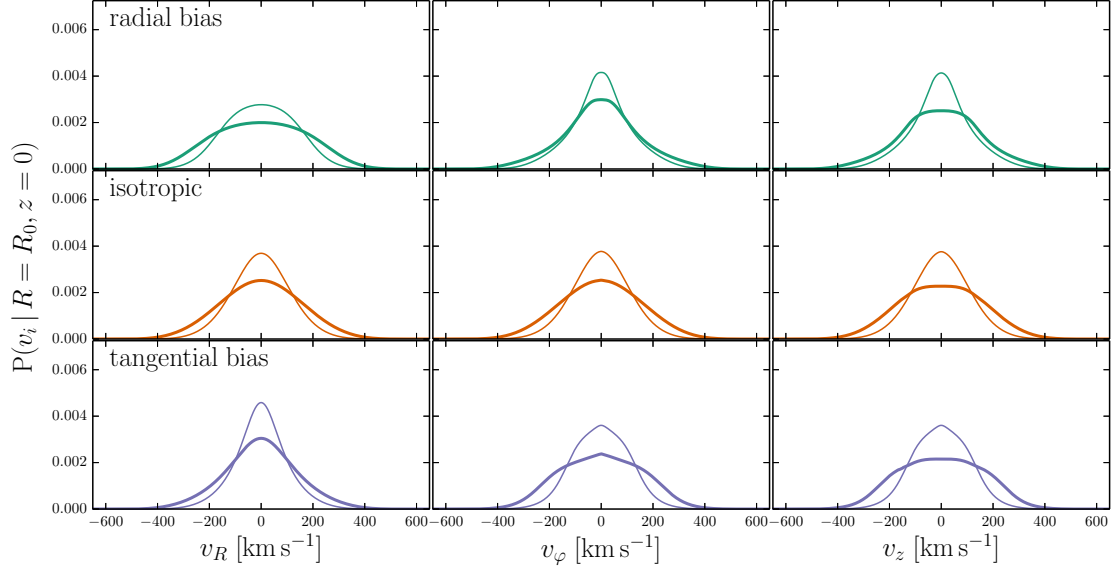


**Figure 8.** Dark matter velocity distribution in the solar annulus for our three halo models.

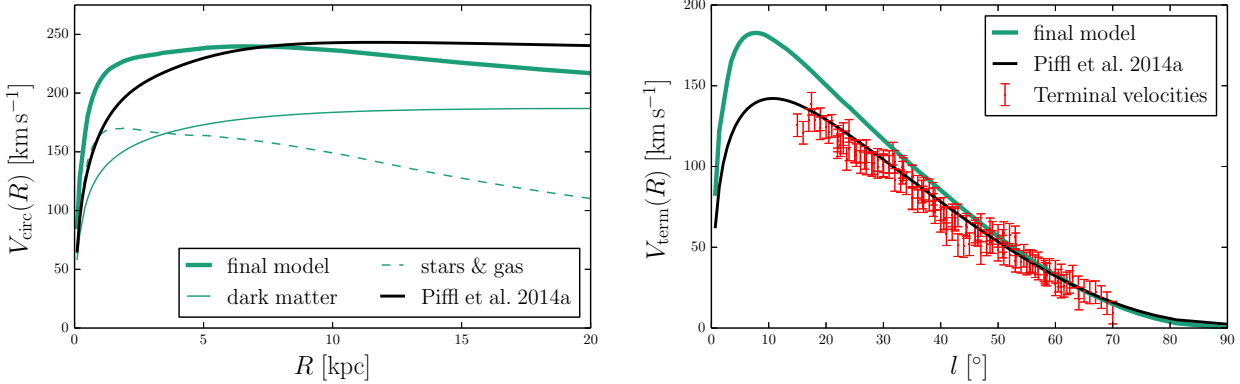


**Figure 11.** Left: Circular speed curve of the target mass distribution (black line) and our final self-consistent model with a radially biased velocity structure in the dark halo. The other two models yield almost indistinguishable curves. The individual contributions from the dark halo and the baryonic component are also shown. Right: Terminal velocity curve as a function of Galactic longitude,  $l$ , predicted by the same models as in the left panel and for comparison the HI terminal velocity measurements from Malhotra (1995) to which the P14 models were fitted.

have seen above the adiabatic contraction of the dark halo significantly alters the halo’s density profile. To counteract these changes as far as possible we re-scaled the halo component such that we still obtained the right circular speed in the solar cylinder, but we clearly cannot expect the circular speed to match perfectly at all other radii.

The extent of the mismatch is illustrated in Fig. 11. On account of the stronger central concentration of the contracted halo, the rotation curve remains flat down to much lower radii (left panel). The right panel shows that such behaviour is not backed up by observations of the motions of the HI gas disc (Malhotra 1995). This is a fundamental problem that ties back to the utilisation of the un-altered NFW profile in the fitting of our target model. This profile was shown to fit well the un-contracted dark halo pro-

files in dark-matter-only simulations, but is unlikely to be a good representation for the dark halo of the Galaxy that was altered during the formation of the stellar disc in its centre. Our work hence re-emphasizes the need to take adiabatic contraction into account when constructing dynamically valid Galaxy models. This will certainly be the next step in the exploitation of the new technology presented in this paper.

## 5 DISCUSSION & CONCLUSIONS

We have shown how to construct fully self-consistent multi-component galaxy models with axisymmetric action-based distribution functions  $f(\mathbf{J})$ . As a worked example we have

taken a Galaxy model presented by P14 and made its dark halo a fully dynamical object, and determined the gravitational potential that is self-consistently generated by the stellar disc and the dark halo in the presence of pre-defined contributions from a gas disc and an axisymmetric bulge.

To make the dark halo a dynamical object, we must select its velocity anisotropy. To this end we have introduced a new family of DFs. We have used the new DFs to explore three options: radially biased, isotropic and tangentially biased dark halos. The first two models bracket the predictions of cosmological dark-matter-only simulations.

The most important change in the final model is the adiabatic compression of the dark halo by the flattened potential of the discs; we can for the first time study this process without drawing on N-body simulations. The contraction has two components. The first component is a spherical shrinkage. At radii  $r \gtrsim 1$  kpc, i.e., roughly outside one disc scale height, this is quite well approximated by the simple formalism of Blumenthal et al. (1986). At smaller radii we find stronger contraction. This is the reverse of what is usually found with N-body simulations, in which generally less contraction is observed than Blumenthal et al. predict (Abadi et al. 2010; Gnedin et al. 2010).

The second component of compression is a pinching towards the plane at radii  $r \lesssim 10$  kpc, which flattens the halo. The extent to which the halo flattens on introduction of the discs depends of its velocity anisotropy in the sense that radial bias maximises the flattening. Our initially spherical, radially biased model deforms to an axis ratio  $q < 0.8$  out to  $\sim 5$  kpc. The tangentially biased halo, by contrast, has  $q \gtrsim 0.9$  at  $r > 0.3$  kpc. This has important consequences, since cosmological simulations predict radially biased configurations. Indeed, the left panel of Fig. 6 shows that in the case of a radially biased dark halo, the difference between the actual, compressed halo and the original spherical halo looks very much like a “dark disc”. A “disc” of this type would be non-rotating, in contrast to a dark disc formed by the capture of satellite halos onto low-inclination orbits followed by tidal shredding (Read et al. 2008, 2009; Ruchti et al. 2014; Read 2014).

Our models yield the detailed velocity distribution of dark-matter particles at the Sun, upon which depends the detectability of dark matter in direct detection experiments. The distributions are distinctly non-Gaussian, being more and less sharply peaked in the tangentially and radially biased models, respectively. Given the tendency of particle detectors to have a threshold speed for detection, the radially biased model offers significantly better chances of detecting dark matter.

Recently, P14 modelled the Galaxy by combining dynamical models of the stellar disc with star counts and the kinematics of RAVE stars to obtain estimates the local dark-matter density. They found that the major model uncertainty was the flattening of the dark halo. The best-fitting local dark-matter density increased with the assumed halo axis ratio  $q$  as  $\propto q^{-0.89}$  (cf. their Fig. 9). Here we find that even if the dark halo were originally spherical, the dark halo must be flattened inside the solar radius  $R_0$ , with  $q = 0.7$  to 0.9. Even though  $q$  varies with radius, this variation is modest within  $R_0$ , the relevant region from the perspective of P14.

Using a very different approach to that of P14, Bien-

aymé et al. (2014) determined the local dark-matter density from a subset of the data used by P14. The local dark-matter densities of these two studies agree for halo axis ratio  $q$  in the range 0.79 to 0.94. It is interesting that this is just the range of axis ratios the present study leads us to expect if the dark halo were spherical before the disc was added.

The DFs of our dark halos were chosen so they generate isolated dark halos that closely follow the NFW profile. When cohabiting with the P14 disc, the halos becomes more centrally concentrated, with the consequence that the final circular-speed curves do not match the data as well as in the target model, where the dark halo has an NFW profile in the presence of the discs and bulge. The models do, however, have appropriate values  $v_c(R_0)$  for the circular speed at the Sun. To match the full terminal-velocity curve one needs to compensate for the increased central concentration of the halos by increasing the disc scale lengths from the values adopted by P14.

We hope soon to report new constraints on the structure of our Galaxy's dark halo obtained by fitting to observational data model Galaxies in which the stellar disc, stellar halo and dark halo are all represented by DFs of the form  $f(\mathbf{J})$ . The time is also ripe to fit such models to data for external galaxies, which a new generation of integral-field spectrographs are making extremely rich. We anticipate that these models will constrain the dark-matter distributions strongly because the stars will be described by either distinct DFs for each observationally distinguishable range of metallicities, or by an “extended distribution function” (Sanders & Binney 2015).

## ACKNOWLEDGEMENTS

We thank the member of the Oxford Galactic Dynamics group for helpful comments and suggestions.

JB was supported by STFC by grants R22138/GA001 and ST/K00106X/1. The research leading to these results has received funding from the European Research Council under the European Union's Seventh Framework Programme (FP7/2007-2013)/ERC grant agreement no. 321067.

## REFERENCES

- Abadi M. G., Navarro J. F., Fardal M., Babul A., Steinmetz M., 2010, MNRAS, 407, 435
- Bienaymé O. et al., 2014, A&A, 571, A92
- Binney J., 2012, MNRAS, 426, 1324
- Binney J., 2014, MNRAS, 440, 787
- Binney J., Tremaine S., 2008, Galactic Dynamics: Second Edition. Princeton University Press
- Binney J. J., Evans N. W., 2001, MNRAS, 327, L27
- Bissantz N., Debattista V. P., Gerhard O., 2004, ApJ, 601, L155
- Blumenthal G. R., Faber S. M., Flores R., Primack J. R., 1986, ApJ, 301, 27
- Combes F., Sanders R. H., 1981, A&A, 96, 164
- Gnedin O. Y., Brown W. R., Geller M. J., Kenyon S. J., 2010, ApJ, 720, L108
- Hansen S. H., Moore B., 2006, New Astronomy, 11, 333

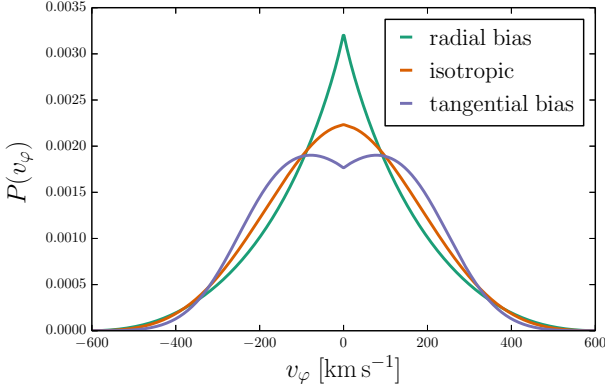


**Figure 12.** Local  $v_\phi$  distributions using a simpler form of the halo DF with a constant anisotropy parameter.

Jurić M. et al., 2008, *ApJ*, 673, 864  
 Ludlow A. D., Navarro J. F., White S. D. M., Boylan-Kolchin M., Springel V., Jenkins A., Frenk C. S., 2011, *MNRAS*, 415, 3895  
 Malhotra S., 1995, *ApJ*, 448, 138  
 Mo H. J., Mao S., White S. D. M., 1998, *MNRAS*, 295, 319  
 Navarro J. F., Frenk C. S., White S. D. M., 1996, *ApJ*, 462, 563  
 Piffl T. et al., 2014, *MNRAS*, 445, 3133  
 Pillepich A., Kuhlen M., Guedes J., Madau P., 2014, *ApJ*, 784, 161  
 Pontzen A., Governato F., 2013, *MNRAS*, 430, 121  
 Posti L., Binney J., Nipoti C., Ciotti L., 2014, ArXiv e-prints  
 Raha N., Sellwood J. A., James R. A., Kahn F. D., 1991, *Nature*, 352, 411  
 Read J. I., 2014, *Journal of Physics G Nuclear Physics*, 41, 063101  
 Read J. I., Lake G., Agertz O., Debattista V. P., 2008, *MNRAS*, 389, 1041  
 Read J. I., Mayer L., Brooks A. M., Governato F., Lake G., 2009, *MNRAS*, 397, 44  
 Ruchti G. R., Read J. I., Feltzing S., Pipino A., Bensby T., 2014, *MNRAS*, 444, 515  
 Sanders J. L., Binney J., 2014, ArXiv e-prints  
 Sanders J. L., Binney J., 2015, *MNRAS*  
 Sellwood J. A., McGaugh S. S., 2005, *ApJ*, 634, 70  
 Steinmetz M. et al., 2006, *AJ*, 132, 1645

## APPENDIX: CUSPS AND DIMPLES IN $V_\phi$ DISTRIBUTIONS

To implement velocity anisotropy in our halo DF we did not opt for the simplest possible solution. Here we explain the reasons for this decision. In the DF the two factors  $A$  and  $B$  (Eqs. 6, 7) control the anisotropy of the system by enhancing or suppressing the population of orbits with certain properties. These factors are constant except for very radial orbits. This variation makes  $h(\mathbf{J})$  not a strictly homogeneous function any more, a property that was demanded by Posti et al. (2014) when they proposed this class of DFs.

If we remove the  $\mathbf{J}$  dependency by substituting the tanh

function with unity we obtain  $A = b$  and  $B = 1$  which is sufficient to create an anisotropic model. However, when we examine the tangential velocity distribution of such a model (Fig. 12) we find that in the radially biased model, the distribution in  $v_\phi$  has a cusp at  $v_\phi = 0$ , while in the tangentially biased model it has a dimple at  $v_\phi = 0$ ; only the isotropic model has a  $v_\phi$  distribution of the expected domed shape. The cusp and dimple become more pronounced after adiabatic contraction.

The cusp and the dimple arise because the energy, upon which the ergodic DF of the isotropic model depends, is a quadratic function of  $v_\phi$ , while  $J_\phi = Rv_\phi$  is a linear function of  $v_\phi$ . So when the DF of the isotropic model is written as a function of the actions and then Taylor expanded in  $v_\phi$  at fixed  $\mathbf{x}$ , the linear dependence of  $f$  upon  $v_\phi$  that arises from the dependence of  $f$  on  $J_\phi$  has to be cancelled by linear dependencies of  $J_r$  and  $J_z$  on  $v_\phi$ . If these linear dependencies do not cancel,  $\partial f / \partial v_\phi$  is non-zero at  $v_\phi = 0$ , and  $P_{v_\phi}$  acquires a cusp or a dimple there. Below we show that this delicate cancellation is disturbed by shifting  $b$  from unity.

The derivative of the  $v_\phi$  distribution  $P_{v_\phi}$  plotted in Fig. 8 is

$$\frac{dP_{v_\phi}}{dv_\phi}(v_\phi | \mathbf{x}) = \iint dv_R dv_z \frac{\partial f}{\partial v_\phi} \Big|_{\mathbf{x}}, \quad (10)$$

and

$$\frac{\partial f}{\partial v_\phi} \Big|_{\mathbf{x}} = \left( \frac{\partial f}{\partial J_r} \frac{\partial J_r}{\partial v_\phi} + \frac{\partial f}{\partial J_\phi} \frac{\partial J_\phi}{\partial v_\phi} + \frac{\partial f}{\partial J_z} \frac{\partial J_z}{\partial v_\phi} \right)_{\mathbf{x}}. \quad (11)$$

Now

$$\frac{\partial f}{\partial J_r} = \frac{\partial f}{\partial h(\mathbf{J})} \frac{1}{b} \quad (12)$$

and

$$\frac{\partial f}{\partial J_\phi} = \frac{\partial f}{\partial J_z} = \frac{\partial f}{\partial h(\mathbf{J})} \frac{\Omega_\phi}{\kappa} \quad (13)$$

We require derivatives with respect to  $v_\phi$  at a fixed location  $\mathbf{x} = (R, 0)$  in the plane, so

$$\frac{\partial J_\phi}{\partial v_\phi} = R, \quad (14)$$

where we have used  $J_\phi = Rv_\phi$ .

We don't have analytic expressions for  $\partial J_r / \partial v_\phi$  and  $\partial J_z / \partial v_\phi$ , but the following argument shows that  $\partial J_r / \partial v_\phi < 0$  for  $0 \leq v_\phi \ll v_{\text{circ}}(R)$ . Consider a star with low  $v_\phi$ , and therefore a small guiding radius, that is just able to reach  $(R, 0)$ , i.e. has its apocentre there. It is on an eccentric orbit with substantial  $J_r$ . Increasing  $v_\phi$  moves the guiding centre outwards and thus diminishes the amplitude of the star's radial oscillations and lowers its value of  $J_r$ .

To see that  $\partial J_z / \partial v_\phi |_{\mathbf{x}} < 0$  for  $0 \leq v_\phi \ll v_{\text{circ}}(R)$ , consider the case of a spherical potential. Then  $J_z = L - |J_\phi|$  with  $L = R\sqrt{v_\phi^2 + v_z^2}$  in the Galactic plane, so

$$\frac{\partial J_z}{\partial v_\phi} = \frac{\partial L}{\partial v_\phi} - R = \frac{R^2 v_\phi}{L} - R = R \left( \frac{J_\phi}{L} - 1 \right), \quad (15)$$

which is clearly negative for small  $v_\phi$ . In a strongly flattened potential, the vertical motion largely decouples from the planar motion, so  $\partial J_z / \partial v_\phi$  becomes numerically small, but it remains negative.

Inserting all these insights into equation (11) we arrive at

$$\frac{\partial f}{\partial v_\varphi} = \frac{\partial f}{\partial h(\mathbf{J})} \left( \frac{1}{b} \frac{\partial J_r}{\partial v_\varphi} + \frac{\Omega_\varphi}{\kappa} R + \frac{\Omega_\varphi}{\kappa} \frac{\partial J_z}{\partial v_\varphi} \right) \quad (16)$$

for the integrand in equation (10). Since  $\partial f/\partial h(\mathbf{J}) < 0$ , the sign of  $dP_{v_\varphi}/dv_\varphi$  is opposite to the sign of the bracket in equation (16). In the isotropic case ( $b = 1$ ) we must have  $dP_{v_\varphi}/dv_\varphi \simeq 0$  at  $v_\varphi = 0$ , so

$$\frac{\partial J_r}{\partial v_\varphi} + \frac{\Omega_\varphi}{\kappa} \frac{\partial J_z}{\partial v_\varphi} \simeq -\frac{\Omega_\varphi}{\kappa} R. \quad (17)$$

Hence for  $b \neq 1$  this balance is disturbed with the consequence that  $P_{v_\varphi}$  acquires a non-zero gradient at  $v_\varphi = 0$ , the gradient being negative when  $b > 1$  and positive when  $b < 1$  as is evident in Fig. 12.

While cusps and dimples are not strictly unphysical, we think it unlikely that real dark-matter distributions would exhibit them. A requirement to avoid these features amounts to a restriction on permissible forms of the function  $h(\mathbf{J})$  as, e.g. the one we choose for this work.